CrossMark

Pseudo-outcrop Visualization of Borehole Images and Core Scans

Evgeny M. Mirkes[1] · **Alexander N. Gorban**[1] · **Jeremy Levesley**[1] · **Peter A. S. Elkington**[2] · **James A. Whetton**[2]

Abstract A pseudo-outcrop visualization is demonstrated for borehole and full-diameter rock core images to augment the ubiquitous unwrapped cylinder view and thereby assist nonspecialist interpreters. The pseudo-outcrop visualization is equivalent to a nonlinear projection of the image from borehole to earth frame of reference that creates a solid volume sliced longitudinally to reveal two or more faces in which the orientations of geological features indicate what is observed in the subsurface. A proxy for grain size is used to modulate the external dimensions of the plot to mimic profiles seen in real outcrops. The volume is created from a mixture of geological boundary elements and texture, the latter being the residue after the sum of boundary elements is subtracted from the original data. In the case of measurements from wireline microresistivity tools, whose circumferential coverage is substantially <100 %, the missing circumferential data are first inpainted using multiscale directional transforms, which decompose the image into its elemental building structures, before reconstructing the full image. The pseudo-outcrop view enables direct observation of the angular relationships between features and aids visual comparison between borehole and core images, especially for the interested nonspecialist.

✉ Peter A. S. Elkington
   peter.elkington@weatherford.com

   Evgeny M. Mirkes
   em322@le.ac.uk

   Alexander N. Gorban
   a.n.gorban@le.ac.uk

   Jeremy Levesley
   jl1@le.ac.uk

[1] Department of Mathematics, University of Leicester, Leicester LE1 7RH, UK

[2] Weatherford, East Leake, Loughborough LE12 6JX, UK

1 Introduction

A common starting point for geological analysis of circumferential images from boreholes and full-diameter cores is identification of the types and orientations of bed boundaries and other discontinuities (Rider and Kennedy 2011). Analysts determine the orientation of individual features and examine the ways in which the orientation of successive boundaries evolves over depth to delineate local structures and infer depositional environments. In combination with other data at a variety of scales, image data help refine geological models and define flow units and baffles in reservoir models. Image data also correlate with variations in mineralogy, porosity, and fluid content, making them useful in petrophysical analysis (Xu and Torres-Verdín 2013; Fu et al. 2016). Additional textural information may be available from optical surface scans of full-diameter rock cores; correlating these with borehole images in the same well allows the core and its features to be oriented in the earth's frame of reference via orientation data acquired by the logging tool.

High-resolution borehole images are routinely recorded, yet they are largely underutilized because of a lack of understanding of the data (Joubert et al. 2016). A contributing factor is the way in which the data are visualized; note that similar visualizations are applied to circumferential scans of full-diameter cores. Both types of image are commonly displayed as unwrapped cylinders in which planar features appear as sinusoids, and appropriate software is needed to compute their individual orientations. The cylinder view has the advantage of being straightforward to generate, but it requires a mental transformation to visualize the angular relationships that would be observed in outcrops.

To observe boundary orientations in the earth's frame of reference, a solid volume corresponding to the material removed from the borehole must be constructed and sliced vertically in two planes. Modulating the external dimensions with a proxy for grain size gives a two-sided pseudo-outcrop view in which planar features are seen to be planar (rather than sinusoidal), and the angular relationships between them are observed directly without reference to other plots. All the information available to the reconstruction is located on the borehole wall or core surface; the interior has not been sampled. This differs from the typical three-dimensional (3D) inpainting problem in which the interior of an object is partially sampled. Aspect ratio is another differentiating characteristic, because borehole images are long relative to their diameter. Image logs from a typical 0.2-m-diameter well commonly exceed 1000 m in length; for the datasets examined here, the depth sample increment is 2 mm with 176 circumferential samples. It is desirable to visualize these data quickly.

In the case of wireline tool microresistivity measurements, current flows from individual 4-mm-diameter electrodes arranged in rows and inlaid in pads pressed against the borehole wall (Fig. 1a). In small-diameter wells, the rows overlap circumferentially to give full coverage, but when the well diameter exceeds approximately 150 mm (Fig. 1c), the space between pads creates longitudinal gaps in the image (Fig. 1b). The gaps are bound by linear margins in the tool's frame of reference. Any 3D inpainting
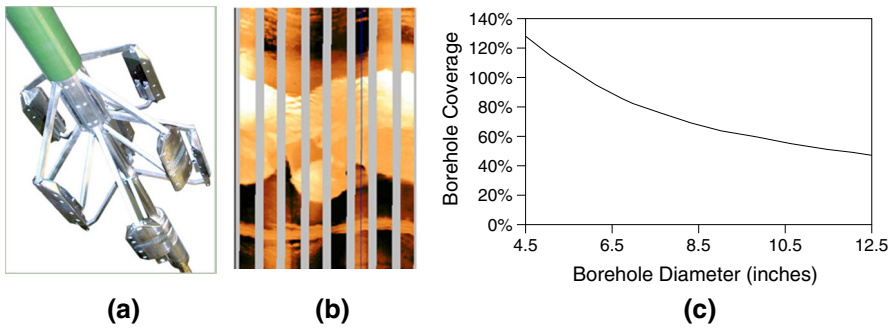
Fig. 1 Microresistivity borehole imaging tool: pad section (**a**), unwrapped image (**b**), and circumferential coverage as function of borehole diameter (**c**)

solution must handle the gaps directly; alternatively, a two-dimensional (2D) inpainting solution must be applied as a preprocessing step.

In general, there are two classes of algorithms for filling holes in digital images: texture synthesis and inpainting (Criminisi et al. 2004). The former has been demonstrated for repeating patterns with some stochasticity, and the latter for linear and curvilinear structures such as object contours. Both classes of algorithm have been applied to borehole images. The statistical properties of the measured parts were used by Hurley and Zhang (2011) to generate realizations for filling the gaps in microresistivity images. This method can be appropriate for images dominated by textural features, such as vugs typical of carbonate rock formations, but achieving continuity across gap boundaries can be problematic, which makes it less well suited to images of rocks with complex curvilinear structures. This limitation is addressed by constraining the selection of realizations with structural information from locally adapted kernel regression (Takeda et al. 2007; Zhang et al. 2016). An inpainting method based on compressed sensing has been shown to successfully reconstruct full circumferential coverage in borehole images with up to 30 % coverage loss and up to 50 % in favorable cases (Assous et al. 2014). The inpainting method builds on the general idea of minimizing the data required to represent information, which it seeks to do with the fewest multiscale directional transform coefficients such that reversing the process recovers the full data, including parts missing from the original samples (Elad et al. 2005). The images are decomposed into elemental building structures (textures and piecewise-smooth parts) that are combined to represent observed features (Starck et al. 2005). This method is well suited to images containing bedding surfaces, fractures, slumps, clasts, and other curvilinear features typical of clastic rock formations and (depending on the choice of directional transform) is also able to handle textural elements.

Two-dimensional inpainting techniques have been extended to three dimensions for a variety of applications. In particular, multipoint geostatistics has been applied to filling gaps in micro-computed tomography scans of porous rocks by extracting characteristics from a training image to generate a database of characteristics from which structures are selected to complete the missing parts in the target image (Zhang and Du 2014). Statistical methods have also been applied to the creation of volumetric textures from 2D samples (Chen and Wang 2010; Urs et al. 2014). The compressed

sensing approach has also been extended to three dimensions; new multiscale directional transforms that enable the true geometry of 3D objects to be captured have been designed (while avoiding the risk of misrepresentation from slice-by-slice processing) (Woiselle et al. 2011).

An alternative method is designed to be useful for images in which the primary structural elements are planar or subplanar at borehole/core scale. This is the case in many hydrocarbon-bearing siliciclastic rocks logged by microresistivity imaging tools. The method will propagate solid textures but not necessarily in an optimal way. It can be easily combined with any advanced method of texture analysis if textural elements are the primary interest (such as in vuggy carbonates). It is tested on several real-life examples.

This paper comprises three sections: "Description of the Method," "Results," and "Conclusions."

2 Description of the Method

The principal steps in constructing the 3D volume are as follows:

1. Divide the log into overlapping depth windows. In each window, identify the dominant set of planar/subplanar geological features and remove them from the image. This is level 1 decomposition.
2. Identify the dominant planar feature set within the residual image and subtract it. This is level 2 decomposition. Repeat the process several times until all of the subsidiary planar geological features are identified and the final residual image contains only nonplanar features. The image may include strongly nonplanar features and a host of other features that are localized azimuthally and will be referred to as residual texture.
3. Identify functions to represent the shape of the primary geological feature and each subsidiary feature for all the levels of decomposition, and use these to construct a synthesized volume.
4. Propagate the residual textures through the volume.

Once created, the volume is visualized by, for example, making two longitudinal cuts through the oriented volume to expose a wedge of material, which allows examination of the orientations of geological features and their relationships in the earth's frame of reference. Additional information from the image measurement can be encoded as variations in the external dimensions of the wedge.

An image of a borehole wall is presented in several coordinate systems in Fig. 2. Let us consider one of the overlapping depth windows as a cylinder (Fig. 2c). Before the earth frame transformation begins, the raw image-log data are processed in the usual way and stored in an array f_{ij}, where $i = 1, \ldots, H$ are rows corresponding to depth and $j = 1, \ldots, N$ are columns corresponding to circumferential location (Fig. 2a). These 2D arrays correspond to the surface of a cylinder (Fig. 2c). The borehole has nominal radius R, and the step between rows is h. Note that the data are discrete with step h in the vertical direction, and f_{ij} is the restriction of a scalar field f to the surface of the borehole. Each position (i, j) in the array f_{ij} corresponds to the space radius-vector $\mathbf{r}_{ij}$ from the origin O to the point on the cylinder surface.

Fig. 2 Standard 2D borehole image (**a**), 2D image after subtraction of the dominant dip sinusoid from the ordinate (**b**), and cylindrical borehole surface in 3D coordinate system (**c**)


(a)   (b)   (c)
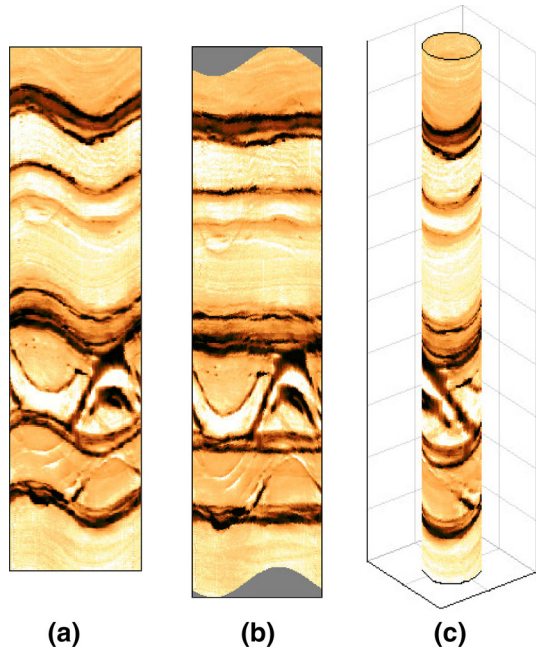
Some of the f_{ij} may correspond to missing or bad measurements, so a mask m_{ij} is used to identify the locations of valid values, in which a value of 1 is used if a given f_{ij} is known and 0 is used if f_{ij} is unknown. At this point it may be advantageous to construct a full circumferential coverage image by application of the morphological components analysis method (Assous et al. 2014).

The planar structure shown in Fig. 3 is an important part of the method. Two angles, ϕ and ψ, describe the planes relative to a reference direction (True North in this case), and a distance coordinate identifies the stack of planes by sequence number. The fragment of the borehole between two neighboring planes is called a *slice*. The polar angle $\phi \in [0, \pi/2]$ is the angle that the normal vector **n** to the planes makes with the vertical axis. The azimuthal angle $\psi \in [0, 2\pi]$ is the angle that the projection of the normal onto the base of the cylinder makes with True North. For the degenerate case of zero ϕ, the value of ψ is set to zero. Three examples illustrate the idea in Fig. 3, with Fig. 3a being a reference configuration. In Fig. 3b an increase in ϕ corresponds to a higher angle of dip, and in (Fig. 3c) the angle ψ has decreased such that the planes have the same dip but the high point of the planes is rotated to a different position. All slices that have substantially the same angles ϕ and ψ are designated as a slice family $S_{\phi\psi}$.

In the Cartesian coordinate system (Fig. 4), the origin O is located at the center of the upper base of a cylinder, the y-axis is directed towards True North, and the x and y coordinates of the point f_{ij} are defined as

$$x_{ij} = R \sin \alpha_j, \quad y_{ij} = R \cos \alpha_j, \tag{1}$$
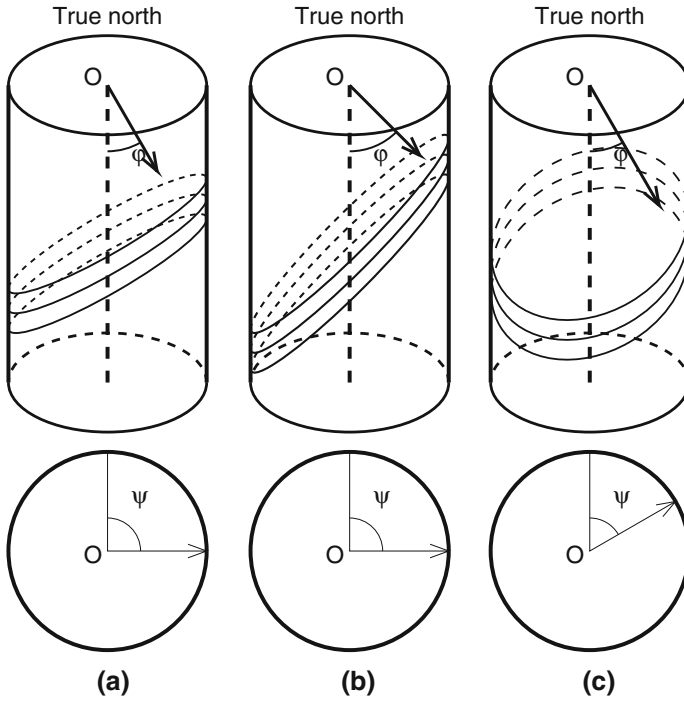
Fig. 3 Reference slope and orientation of planes (**a**), steeper planes with increased ϕ (**b**), and rotated planes with decreased ψ (**c**)

where α_j is the angle between the y-axis and the point f_{ij} for the j column and is defined as

$$\alpha_j = \frac{2\pi j}{N}. \tag{2}$$

The z-axis is directed downward, and the z-coordinate of the point f_{ij} is given by

$$z_{ij} = h(i - 1). \tag{3}$$

Assuming that all slices in the family have the same constant thickness equal to the spacing h between adjacent members of the slice family, it is possible to enumerate the slices in the slice family by distance from the origin O. The Cartesian form of the unit normal vector **n** is

$$x_n = \sin \phi \sin \psi, \quad y_n = \sin \phi \cos \psi, \quad z_n = \cos \phi. \tag{4}$$

The directed length of the projection of the vector $\mathbf{r}_{ij}$ on the unit normal vector is the dot product of the unit normal vector **n** and the vector $\mathbf{r}_{ij}$

$$p_{ij} = \mathbf{n} \cdot \mathbf{r}_{ij} = R \sin \phi \cos(\psi - \alpha_j) + h(i - 1) \cos \phi. \tag{5}$$
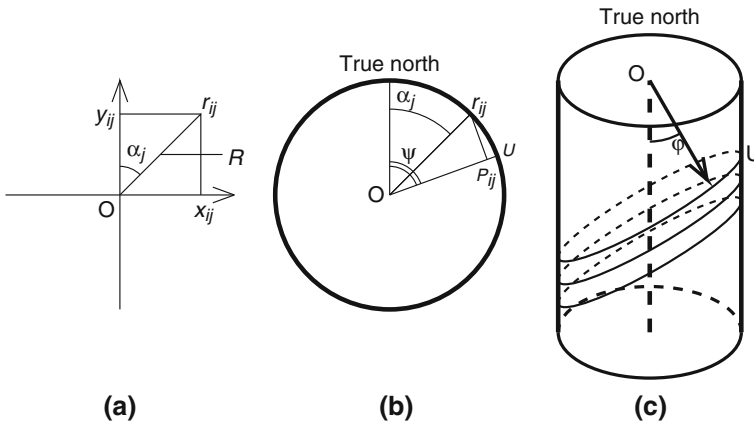
Fig. 4 Cartesian coordinate system (**a**), True North reference (**b**), and planar slices (**c**)

The enumeration of the slice is then this length divided by the depth of one slice h

$$v_{ij} = \left[\frac{p_{ij}}{h}\right] = \left[\frac{R}{h} \sin\phi \cos(\psi - \alpha_j) + (i-1)\cos\phi\right], \qquad (6)$$

where $[\cdot]$ is rounding to the nearest integer. This describes the slice family and the number of the slice within the family.

All points in slice p of an ideal slice family have the same value $\overline{f(p)}$. The best set of planes is computed by minimizing the variance of the residual of the actual data after subtraction of the approximation

$$V(\phi, \psi) = \text{var}(f, S_{\phi\psi}) = \frac{1}{\sum_{ij} m_{ij}} \sum_{m_{ij}=1} \left(f_{ij} - \overline{f(v_{ij})}\right)^2. \qquad (7)$$

It can be easily shown that the optimal slice constant $\overline{f(p)}$ is the mean of all points f_{ij} of this slice

$$\overline{f(p)} = \frac{\sum_{v_{ij}=p,\, m_{ij}=1} f_{ij}}{\sum_{v_{ij}=p} m_{ij}}. \qquad (8)$$

Three images of real borehole walls were selected for the case study (Fig. 5a–c). The initial images, the dominant dip sets, the dominant dip sets plus second-, third-, and fourth-level dips, and sums of dip sets plus residual texture (the "total" column) are presented in Fig. 5 for all cases. The model slice family is found by minimizing the expression (7) over all polar and azimuthal angles. Surfaces of this function, which depends on a particular choice of angles, are presented in Fig. 6 for borehole walls from Fig. 5. The second (local) minimum on the bottom surface corresponds approximately to the second dip of the case in Fig. 5c. There appear no problems discretizing the slices when they are parallel to the borehole because of convenient parameterization. The Nelder–Mead algorithm (Algorithm 1) (Nelder and Mead 1965) is used with
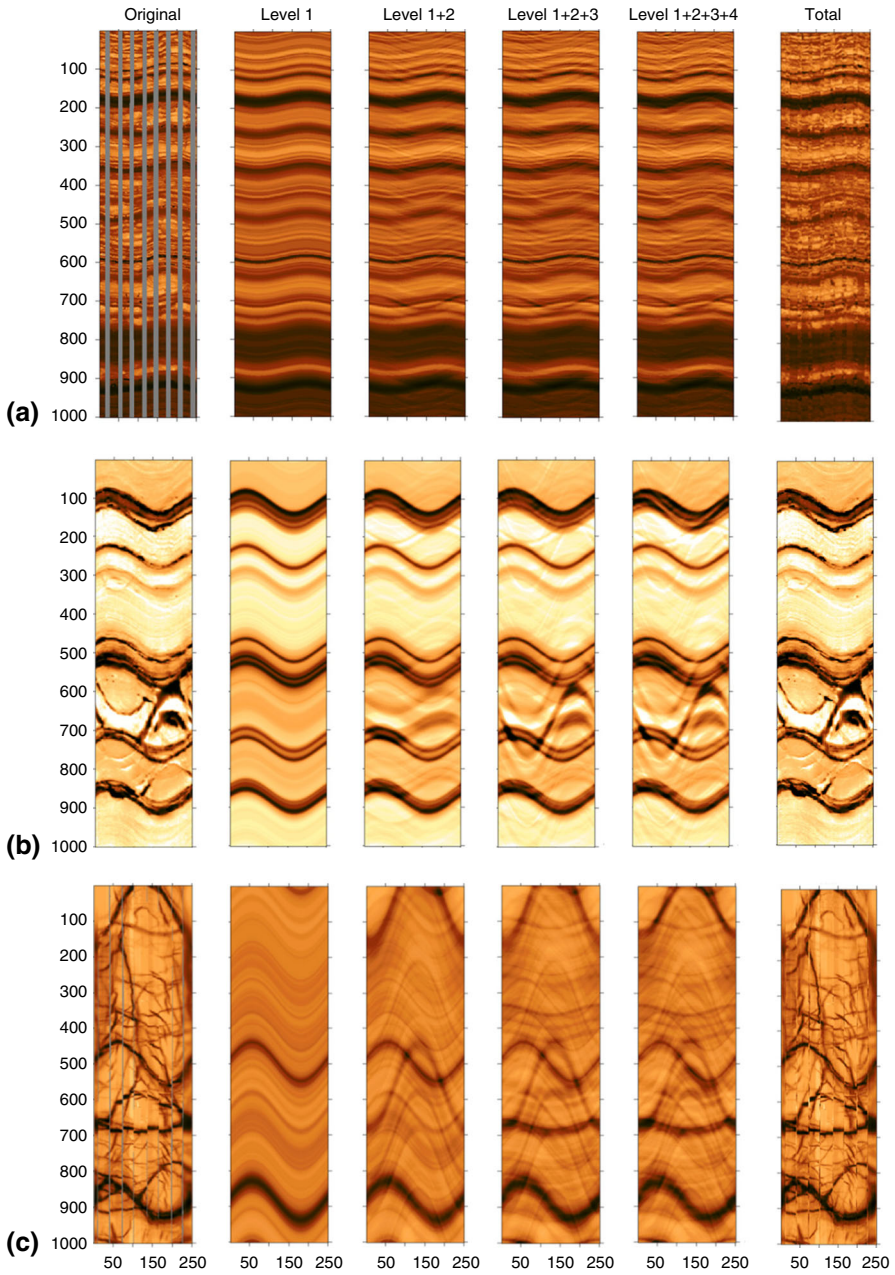
Fig. 5 Three images for the case study: image with 65 % circumferential coverage (**a**), 65 % circumferential coverage, two-dimensionally inpainted (**b**), and 95 % coverage (**c**)
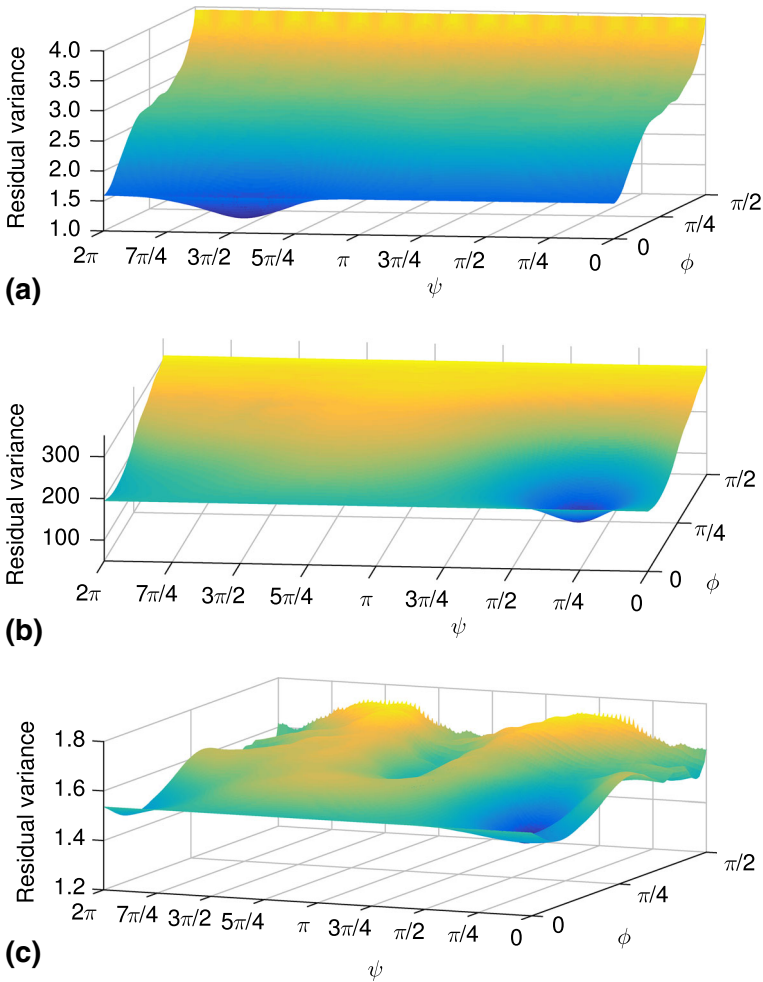
Fig. 6 Two-dimensional plots of variance of residual (7) for the dominant dip calculated for the borehole wall images in Fig. 5a–c (in the same order)

several random starts to seek the minimum of the residual (7). The random starts were repeated until the best solution appeared twice within specified accuracy. Practically, the global minimum of the residual variance has a large domain of attraction and minimization is not significantly difficult or computationally expensive if the depth of the window exceeds its circumference (the width). If the aspect ratio approaches 1 (a rare situation), then the optimization landscape becomes more noisy and a special smoothing is needed for optimization. If the optimization landscape is smooth (Fig. 6) and the domain of attraction for the global minimum is large, then the solution of the optimization problem is expected to be robust with respect to small perturbations.

Algorithm 1 Minimization of function $V(\phi, \psi)$ (7)

1: $\alpha \leftarrow 1, \beta \leftarrow 2, \gamma \leftarrow 0.5, \sigma \leftarrow 0.5$ ▷ Initiate parameters of the Nelder–Mead algorithm
2: $\psi_1 \leftarrow 0, \phi_1 \leftarrow 0, V^* \leftarrow 2V(0,0), \varepsilon \leftarrow 0.0001$ ▷ Initiate search parameters
3: **repeat**   ▷ Search of the second case of the best solution within specified accuracy
4:     **if** $V^* > V(\psi_1, \phi_1)$ **then**
5:        $\psi^* \leftarrow \psi_1, \phi^* \leftarrow \phi_1, V^* \leftarrow V(\psi_1, \phi_1)$ ▷ Save the best solution
6:     $\psi_1 \leftarrow 2\pi r_1, \phi_1 \leftarrow \pi r_2/2$ ▷ Generate center of simplex; r_1, r_2 are random numbers
7:     $\psi_2 \leftarrow \psi_1 + \pi, \phi_2 \leftarrow \phi_1, \psi_3 \leftarrow \psi_1, \phi_3 \leftarrow \phi_1 + \pi/4$ ▷ Complete simplex
8:     **repeat**   ▷ the Nelder–Mead search for specified initial point
9:        Sort vertices to hold $V(\psi_1, \phi_1) \leq V(\psi_2, \phi_2) \leq V(\psi_3, \phi_3)$ ▷ Ordering
10:       $\psi_c \leftarrow (\psi_1 + \psi_2)/2, \phi_c \leftarrow (\phi_1 + \phi_2)/2$ ▷ Centroid calculation
11:       $\psi_r \leftarrow \psi_c + \alpha(\psi_c - \psi_3), \phi_r \leftarrow \phi_c + \alpha(\phi_c - \phi_3)$ ▷ Calculate reflection point
12:       **if** $V(\psi_1, \phi_1) \leq V(\psi_r, \phi_r) < V(\psi_2, \phi_2)$ **then**
13:          $\psi_3 \leftarrow \psi_r, \phi_3 \leftarrow \phi_r$ ▷ Reflection
14:       **else if** $(V(\psi_r, \phi_r) \leq V(\psi_1, \phi_1))$ **then**
15:          $\psi_e \leftarrow \psi_c + \beta(\psi_r - \psi_c), \phi_e \leftarrow \phi_c + \beta(\phi_r - \phi_c)$ ▷ Calculate expansion point
16:          **if** $(V(\psi_e, \phi_e) \leq V(\psi_r, \phi_r))$ **then**
17:             $\psi_3 \leftarrow \psi_e, \phi_3 \leftarrow \phi_e$ ▷ Expanding
18:          **else**
19:             $\psi_3 \leftarrow \psi_r, \phi_3 \leftarrow \phi_r$ ▷ Reflection
20:       **else**   ▷ Now $V(\psi_r, \phi_r) \geq V(\psi_2, \phi_2)$
21:          $\psi_{co} \leftarrow \psi_c + \gamma(\psi_3 - \psi_c), \phi_{co} \leftarrow \phi_c + \gamma(\phi_3 - \phi_c)$ ▷ Calculate contraction point
22:          **if** $V(\psi_{co}, \phi_{co}) \leq V(\psi_3, \phi_3)$ **then**
23:             $\psi_3 \leftarrow \psi_{co}, \phi_3 \leftarrow \phi_{co}$ ▷ Contracting
24:          **else**
25:             $\psi_j \leftarrow \psi_1 + \sigma(\psi_j - \psi_1), \phi_j \leftarrow \phi_1 + \sigma(\phi_j - \phi_1), j = 2, 3$ ▷ Shrinking
26:     **until** $\min_{i,j} |\psi_i - \psi_j| \leq \varepsilon$ and $\min_{i,j} |\phi_i - \phi_j| \leq \varepsilon$
27: **until** $|\psi^* - \psi_1| \leq \varepsilon$ and $|\phi^* + \phi_1| \leq \varepsilon$

After finding the best slice family, the residual field is computed by subtracting the values on the slice family found from the known field f

$$\text{res}^1_{ij} = f_{ij} - s^1_{ij}, \forall m_{ij} = 1,$$

where s^1_{ij} is the value of approximation of the field f at the point ij by the best slice family. This value is equal to $\overline{f(v_{ij})}$. The secondary slice structure s^2 is found by repeating the same procedure for the residual random field r^1 instead of f. Thus, recursively a sequence of layers $s^1, s^2, \ldots, s^L$ can be removed until the statistics of the residual are more or less random (or at a user-selected level), leaving behind a field that is considered to be residual texture, denoted by t_{ij}.

One value of the field is assigned per slice. This is the mean of all values f_{ij} of this slice $\overline{f(p)}$. This value is considered as a constant when extended in the modeled volume. For each $k = 1, \ldots, L$, the slice s^k is inpainted by this value inside the cylinder. These functions $s^k(x, y, z)$ are called below the *boundary elements*. The boundary element $s^{k+1}(x, y, z)$ provides the best approximation of the residual

$$\text{res}^k_{ij} = f_{ij} - \sum_{q=1}^{k} s^q_{ij} \tag{9}$$
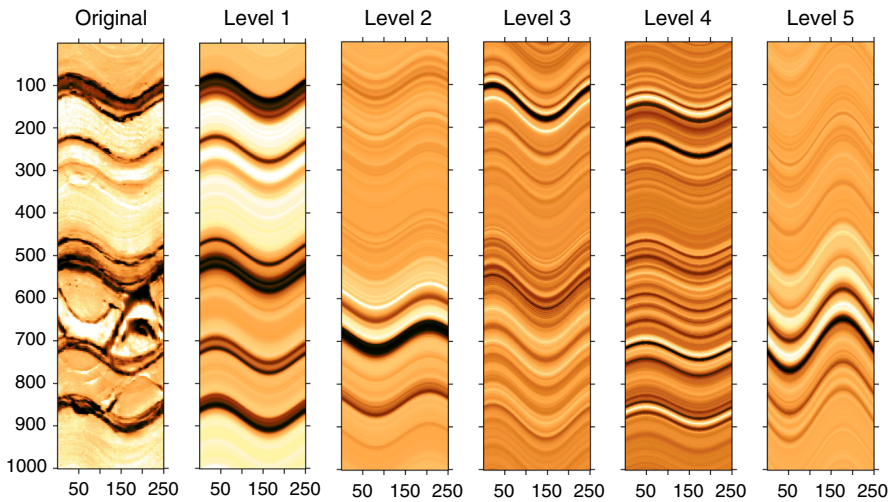
Fig. 7 Original image and different levels s^k ($k = 1, \ldots, 5$) of the decomposition for the case in Fig. 5b. The values of s^k are rescaled to the standard maximum and minimum

on the cylinder boundary by the function, which is constant in every slice from a system of parallel slices. The approximation of the image is a sum of these boundary elements (9). This sum is not constant in any slice for $k > 1$ for a general situation when the original field f_{ij} is not constant in a slice.

The first level s^1 in Fig. 5 (the second column) dominates in the decomposition. Figure 7 concerns the case in Fig. 5b. It represents the information brought from each level separately for five levels. In this case, the variance of s^k for $k > 1$ is much less than the variance of s^1. The residuals after subtraction of the approximations of various levels for the same real-life case are presented in Fig. 8. The variance of the residual decreases at each step. The final residual is used for generation of the residual texture. It is clear from Fig. 8 that, in this example, the residual does not change significantly after the third step.

To compute a value inside the volume, it is sufficient to identify the appropriate slices to which the point belongs at each level of this decomposition and then to compute the value of the residual texture inside the volume. For this purpose, modeling of residual texture as a 3D moving average field (Francos and Friedlander 1998; Ojeda et al. 2010) is employed with calibration of the results to the observed statistics on the boundary of the borehole. Autocorrelations of this field are evaluated by its boundary values and are used for continuation of the field inside the volume.

The problem of selecting the best number of boundary elements is very similar to the problem of selecting the number of principal components in signal approximation, and there are several useful heuristics for its solution Cangelosi and Goriely (2007). Usually, the first 3–5 boundary elements approximate the field quite well, and the rest is left for the random field of texture. In Fig. 9, fraction of variance unexplained (FUV) plots are presented as a function of the number of layers for the images used in the case study (Fig. 5). The variance of the residual decreases monotonically, but this decrease
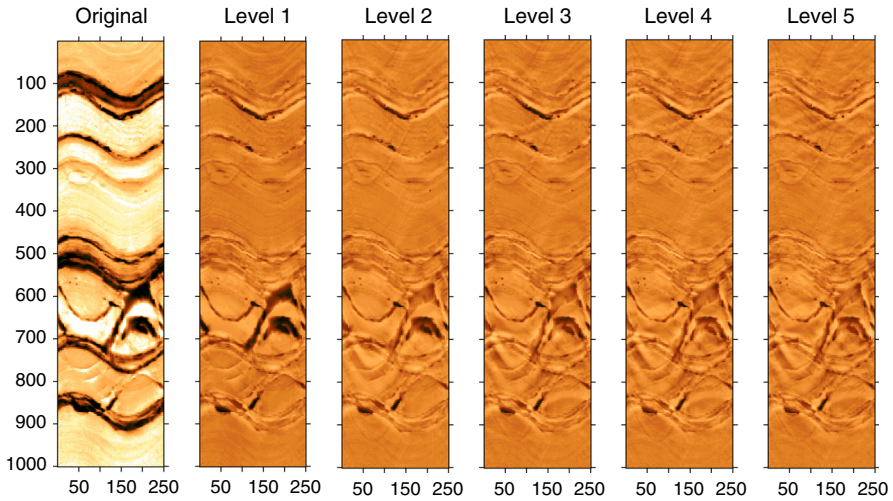
Fig. 8 Original image and residuals res^k ($k = 1, \ldots, 5$) after extraction of the approximations. The values of res^k are rescaled to the standard maximum and minimum
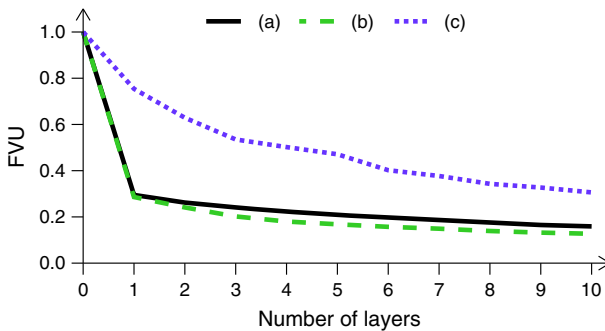
Fig. 9 FUV plots for the images presented in Fig. 5 as a function of number of slices used

could be slow (see Fig. 8, where the difference between level 4 and level 5 residuals is not obvious).

This version of our algorithm seeks planar dominant features, but in principle, other geological features might be identified. Subtracting these from the original data leaves the subsidiary (i.e., less geologically significant) features which are isolated by an iteration of the method. Each set of subsidiary features is subtracted from the remaining data, and the process is repeated to isolate all of the significant subsidiary sets. A quality-of-fit test is performed on each slice family as it is identified. Examples of the sum of two-, three-, and four-slice families are presented in the corresponding columns of Fig. 5.

To create the synthesized volume representing the rock removed during creation of the borehole, the main function, the $2, \ldots, L$ subsidiary functions, and the residual texture are summed in accordance with the expression

$$\hat{f}_{ij} = \sum_{l=1}^{L} s_{ij}^l + t_{ij}. \tag{10}$$

This equation is termed the reconstruction algorithm and is exact on the boundary. Moreover, for an arbitrary internal point of the cylinder $p = (x, y, z)$, the angle α is calculated as

$$\alpha = \arctan(y/x) \tag{11}$$

(that being an analogue to α_j in Fig. 4a), then the number of the slice in each slice family k is calculated as

$$\nu^k = \left[\frac{R \sin \phi^k \cos(\psi^k - \alpha) + z \cos \phi^k}{h} \right], \tag{12}$$

where ϕ^k and ψ^k are the angles that specify the slice family at level k. Then, Eq. (10) is used to calculate the value of the field at this point.

The model matches the empirical boundary values exactly and preserves the statistical properties of the residual texture inside the volume. This internal residual texture is referred to as t. If necessary, this model can be improved by a multidimensional autoregressive moving average approach or other texture analysis algorithm. There are many geological events which could be classified as texture. Most of them have specific geometries and may require specific tools for modeling. All these algorithms may be applied after extraction of the planar layer structure.

The simple and universal moving average (MA) field is used for the modeling of residuals. Let the residual field $\text{res}_{ij} = \text{res}_{ij}^k$ (9) on the cylindric surface be given. A MA field $T(x, y, z)$ is constructed by averaging of 3D white noise in a sliding window. The sliding window is selected in the form of a rectangular parallelepiped in such a way that the horizontal and vertical correlation radii of $T(x, y, z)$ coincide with the correlation radii of the residual res_{ij} evaluated on the surface. After finding the dominant dip for the positive squared residual field res_{ij}^2, the field res_{ij} is considered in the corresponding slices ν. The mean $\mu(\nu)$ and variance $\sigma^2(\nu)$ of res_{ij} are evaluated in each slice ν. The values of $T(x, y, z)$ are shifted and scaled in each slice ν to have the same mean $\mu(\nu)$ and variance $\sigma^2(\nu)$. The result is used for the inpainting of the texture.

This approach works satisfactorily if the residuals res_{ij}^k are small enough with respect to the layer structure (Fig. 8). If necessary, the model could be refined by using more advanced MA and autoregressive models (Francos and Friedlander 1998; Ojeda et al. 2010) or other universal approaches, including wavelet analysis and its various generalizations (Portilla and Simoncelli 2000), adapted kernel regression methods (Zhang et al. 2016), and methods from statistical physics (Wang et al. 2017), among others. If the residual is not small, then the (multi)layer structure $\sum_{l=1}^{L} s_{ij}^l$ is not dominant in Eq. (10) and special tools for recognition and modeling of geological structures may be needed.

The orientation of the structural or sedimentary structures may not be constant over the window; in addition, the well path can also vary, thus one cannot expect that the
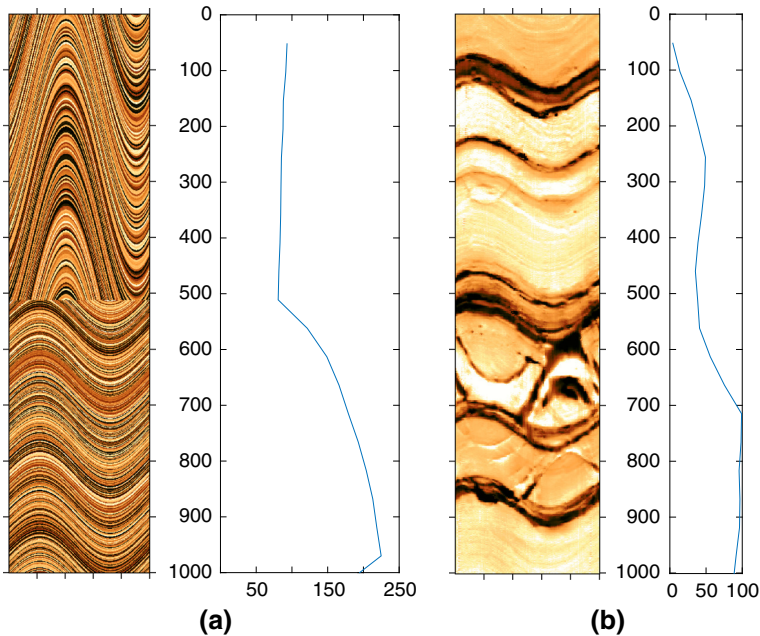
Fig. 10 Dependence of variance of residual (7) (ordinate) on depth of window z (abscissa) for the dominant dip: (**a**) artificial combination and (**b**) the real case in Fig. 5b

sinusoids for a sufficiently long borehole will be strictly parallel. If the change of direction in the sliding window is significant, then a special *segmentation procedure* is needed. Fix a sliding window of the total depth d, with internal coordinate $z \in [0, d]$. Find the optimal dominant dip in a shorter sliding window $[0, z]$ and calculate the variance of residual (7) for this optimal approximation as a function of z: $v(z)$. If this function does not vary from a constant beyond a preselected *tolerance level ε*, then no segmentation is needed. If $v(z)$ deviates from the constant average value by more than ε and a significant slope appears, then segmentation is necessary and the point of segmentation is the break point of the optimal piecewise-linear approximation of $v(y)$. For a detailed description of segmentation algorithms, refer to the classical review by Keogh et al. (2004). Examples of the function $v(y)$ for the borehole images are presented in Fig. 10 for two nonuniform images with segment infrastructure: an artificial combination of two segments (Fig. 10a) and a real example with variable structure (Fig. 10b) taken from Fig. 5b. The segmentation algorithm utilizes the same calculation of residuals and search of optimal dips as the basic approximation algorithm does.

Selection of parallel planar slices for the boundary elements formalizes the idea about planar geological structures. The choice of slices can be modified; For example, instead of parallel planes the families of planes can be considered, which include a given straight line outside the cylinder. In this case, instead of the 2D optimization problem for function (7) on a hemisphere of normal vectors **n**, one has to solve the four-dimensional optimization problem in the space of straight lines. Algebraic surfaces
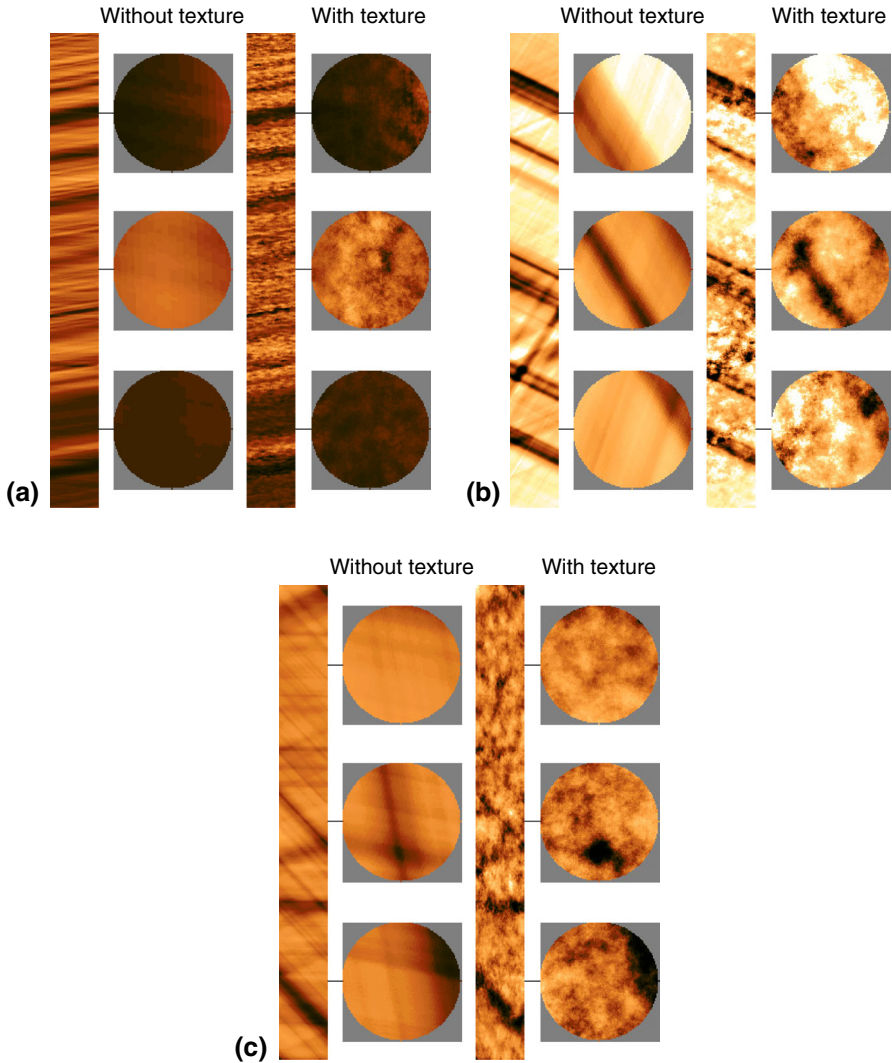
Fig. 11 Vertical and horizontal cross-sections at three different depths reconstructed from the images in Fig. 5a–c in the same order, with and without texture

provide many other possible choices of the families of slices, but introduction of each sophisticated construction needs reasonable geological justification.

3 Results

Figure 5 shows three examples of surface reconstruction from initial images with different circumferential coverage states. The starting point for the upper set of images is Fig. 5a with 65 % coverage, typical of a well drilled with a 203-mm (8-inch) bit.

Borehole View   Outcrop View


(a)   (b)

Successive slice families are shown in Fig. 5b–e, and Fig. 5f shows the reconstruction formed from the sum of slice families plus residual texture. The reconstructed image has all of the main geological features of the original and has additionally filled the gaps present in the initial image. Filling the gaps in this way has introduced some noise. The middle set of images is from another part of the same well, but this time the initial image from Fig. 5a has been inpainted with the morphological components analysis method of Assous et al. (2014), which reconstructs data missing in the gaps without introducing noticeable noise. The lower set of images is from a well drilled with a smaller bit, and the circumferential coverage is 100%. This example includes many fine fractures in addition to the crossing of planar bed boundaries.

Figure 11 shows horizontal and vertical slices through the solid images reconstructed from the images in Fig. 5. For each case, inpainted images with and without texture are presented.

Figure 12 shows an initial image with surface inpainting displayed in the conventional cylinder view and also a solid volume view created by taking two orthogonal slices. Note that the planar geological features appear as curves on the conventional view, and as planes in the solid volume view. Relative to the conventional view, therefore, the angular relationships between geological features in the solid volume view are more straightforward for nonexpert interpreters to understand.

Finally, the method was applied to circumferential scans of fullbore core (Fig. 13). In this case, the external surface of the solid volume has been modulated with a function of the grey level as a proxy for grain size (an indicator of depositional environment

Fig. 13 Fullbore core surface
scan (**a**) and pseudo-outcrop
visualization (**b**)

(a)   (b)
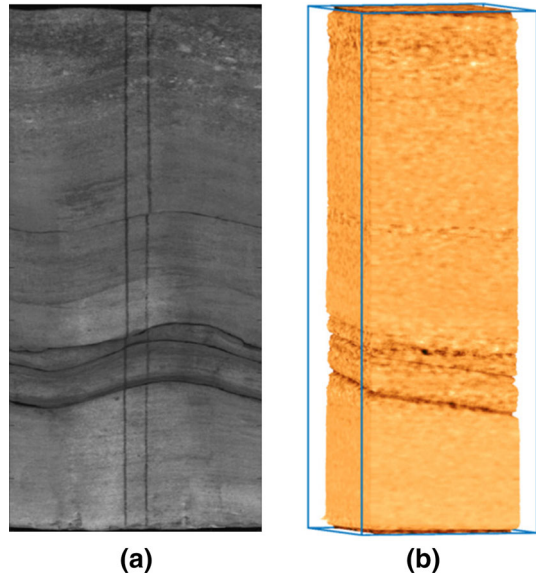
in sedimentary rocks). In the case of microresistivity images, a modulation based on resistivity value can be used.

4 Conclusions

Image volumes created from circumferential microresistivity borehole images and optical core scans have been used to create pseudo-rock outcrop visualizations to help nonexpert interpreters understand the earth-frame angular relationships between geological features. Modulating the external dimensions of the volume with a proxy for grain size adds information indicating depositional environment. The method focuses on planar geological features and textures, but it could be developed to include more complex structures. The method has been demonstrated on images with 65% circumferential coverage, typical of images acquired with pad-based sensors.

References

Assous S, Elkington P, Whetton J (2014) Microresistivity borehole image inpainting. Geophysics 79:D31–D39. doi:10.1190/geo2013-0188.1

Cangelosi R, Goriely A (2007) Component retention in principal component analysis with application to cDNA microarray data. Biol Direct 2:2. doi:10.1186/1745-6150-2-2

Chen J, Wang B (2010) High quality solid texture synthesis using position and index histogram matching. Vis Comput 26:253–262. doi:10.1007/s00371-009-0408-3

Criminisi A, Pérez P, Toyama K (2004) Region filling and object removal by exemplar-based image inpainting. IEEE Trans Image Process 13:1200–1212. doi:10.1109/TIP.2004.833105

Elad M, Starck JL, Querre P, Donoho DL (2005) Simultaneous cartoon and texture image inpainting using morphological component analysis (MCA). Appl Comput Harmon Anal 19:340–358. doi:10.1016/j.acha.2005.03.005

Francos JM, Friedlander B (1998) Parameter estimation of two-dimensional moving average random fields. IEEE Trans Signal Process 46:2157–2165. doi:10.1109/78.705427

Fu HC, Zou CC, Li N, Xiao CW, Zhang CS, Wu XN, Liu RL (2016) A quantitative approach to characterize porosity structure from borehole electrical images and its application in a carbonate reservoir in the Tazhong area, Tarim basin. SPE Reserv Eval Eng. doi:10.2118/179719-PA

Hurley NF, Zhang T (2011) Method to generate full-bore images using borehole images and multipoint statistics. SPE Reserv Eval Eng 14:204–214. doi:10.2118/120671-PA

Joubert JB, Millot P, Montaggioni P, Dymmock S, Andonof L, Kadri N, Torres D (2016) Understanding wireline borehole image workflows from the wellsite to the end user. First Break 34:65–78

Keogh E, Chu S, Hart D, Pazzani M (2004) Segmenting time series: a survey and novel approach. In: Last M, Kandel A, Bunke H (eds) Data mining in time series databases. World Scientific, Singapore, pp 1–22

Nelder JA, Mead R (1965) A simplex method for function minimization. Comput J 7:308–313. doi:10.1093/comjnl/7.4.308

Ojeda S, Vallejos R, Bustos O (2010) A new image segmentation algorithm with applications to image inpainting. Comput Stat Data Anal 54:2082–2093. doi:10.1016/j.csda.2010.03.021

Portilla J, Simoncelli EP (2000) A parametric texture model based on joint statistics of complex wavelet coefficients. Int J Comput Vis 40:49–70. doi:10.1023/A:1026553619983

Rider M, Kennedy M (2011) The geological interpretation of well logs, 3rd edn. Rider-French Consulting Limited, Sutherland

Starck JL, Elad M, Donoho DL (2005) Image decomposition via the combination of sparse representations and a variational approach. IEEE Trans Image Process 14:1570–1582. doi:10.1109/TIP.2005.852206

Takeda H, Farsiu S, Milanfar P (2007) Kernel regression for image processing and reconstruction. IEEE Trans Image Process 16:349–366. doi:10.1109/TIP.2006.888330

Urs RD, Da Costa JP, Germain C (2014) Maximum-likelihood based synthesis of volumetric textures from a 2D sample. IEEE Trans Image Process 23:1820–1830. doi:10.1109/TIP.2014.2307477

Wang H, Wellmann J, Li Z, Wang X, Liang R (2017) A segmentation approach for stochastic geological modeling using hidden Markov random fields. Math Geosci 49:145–177. doi:10.1007/s11004-016-9663-9

Woiselle A, Starck JL, Fadili J (2011) 3-d data denoising and inpainting with the low-redundancy fast curvelet transform. J Math Imaging Vis 39:121–139. doi:10.1007/s10851-010-0231-5

Xu C, Torres-Verdín C (2013) Pore system characterization and petrophysical rock classification using a bimodal Gaussian density function. Math Geosci 45:753–771. doi:10.1007/s11004-013-9473-2

Zhang T, Du Y (2014) A multiple-point geostatistical reconstruction method of porous media using soft data and hard data. J Comput Inf Syst 10:7213–7224. doi:10.12733/jcis11741

Zhang T, Gelman A, Laronga R (2016) Structure and texture-based fullbore image reconstruction. Math Geosci 48:1–21. doi:10.1007/s11004-016-9649-7